

Angle-Resolved Spectroscopy of Parametric Fluorescence

Feng-Kuo Hsu and *Chih-Wei Lai

Department of Physics and Astronomy,

*Michigan State University, East Lansing, MI 48824**

(Dated: February 26, 2013)

Abstract

The parametric fluorescence from a nonlinear crystal forms a conical radiation pattern. We measure the angular and spectral distributions of parametric fluorescence in a beta-barium borate crystal pumped by a 405-nm diode laser employing angle-resolved imaging spectroscopy. The experimental angle-resolved spectra and the generation efficiency of parametric down conversion are compared with a plane-wave theoretical analysis. The parametric fluorescence is used as a broadband light source for the calibration of the instrument spectral response function in the wavelength range from 450 to 1000 nm.

PACS numbers: 42.65.Lm, 42.50.Ct

*Electronic address: cwlai@msu.edu

I. INTRODUCTION

Signal-idler photon pairs generated by spontaneous parametric down-conversion (SPDC) have been used to address fundamental issues of quantum theory and have found application in quantum entanglement and quantum information processing and metrology [1–4]. The SPDC process, also known as parametric fluorescence or parametric scattering [5–10], is a second-order optical process in which a driving pump photon is scattered into signal-idler photon pairs subject to energy and momentum conservation. This spontaneous parametric emission can be described properly only by field quantization. Since its prediction and observation in the 1960s, parametric fluorescence has become a technique for measuring second-order nonlinear susceptibilities [10–13] and for developing tunable light sources via parametric oscillation or amplification processes. In 1969, Zeldovich and Klyshko [14] first proposed the use of parametric fluorescence (luminescence) as a nonclassical source of photon pairs. This description was experimentally verified by Burnham et al. in 1970 [15].

The possible wave vectors of the signal-idler photon pairs are determined by energy and momentum conservation, a constraint referred to as phase-matching, leading to highly directional parametric emission. The phase-matching condition frequently cannot be met for specific wavelengths of interest or practical applications owing to the limited tunability of inherent dispersion of nonlinear materials. However, it can be met by selecting polarization birefringent crystals with appropriate refractive indices or by designing waveguides or periodic structures of specific wavelengths. There are two major types of polarization phase-matching schemes for parametric down-conversions: Type-I, where signal-idler photons have the same polarization (co-linearly polarized photons), and Type-II, where the signal-idler photons have orthogonal polarization (cross-linearly polarized photons). Both types of parametric processes have been used to generate photon pairs, sometimes referred to as biphoton states, which exhibit correlation/entanglement for variables including polarization, momentum, time, energy, and angular momentum.

When the phase-matching condition is met, the signal and idler radiation form a conical pattern independent of the intensity of the pump source. The angular distribution of parametric fluorescence is determined by the energy of the pump, signal, and idler waves, subject to the dispersion of the crystal and walk-off angles of these three waves. The magnitude of the second-order nonlinear susceptibility $\chi^{(2)}$ is a typical selection criterion for parametric downconversion. Many uniaxial or biaxial nonlinear crystals have been used for parametric down conversion: for example, KD*P (potassium dideuterium phosphate, KD_2PO_4), BBO (beta-barium borate, $\beta - \text{BaB}_2\text{O}_4$),

and LBO (lithium niobate, LiNbO_3). In this report, we use BBO, a negative uniaxial class 3m crystal characterized by a wide range of transparency over the ultraviolet ($\lambda \approx 200\text{nm}$) to the infrared ($\lambda \approx 3500\text{nm}$) portion of the spectrum [16]. BBO crystals have been widely studied for harmonic frequency generation, optical parametric oscillation, and generation of bi-photon states.

II. EXPERIMENTAL METHODS

We measure the angular distribution and photon flux of parametric fluorescence from a 3-mm thick BBO crystal. The BBO crystal is cut at an angle of $\theta_m = 29 \pm 0.5^\circ$ with respect to the optical axis. This cut angle θ_m is chosen for the Type-I ($e \rightarrow o + o$) degenerate parametric down-conversion at $\lambda = 810\text{ nm}$ with a pump $\lambda_p = 405\text{ nm}$. The crystal is mounted on a three-axis rotary mount with the crystal's optical axis (OA) in the horizontal plane. The angle formed by the OA and the pump's propagation wave vector can be finely tuned by tilting the crystal to satisfy the phase-matching condition for various θ_m near the crystal cut angle. We can thus adjust the pump and signal Poynting vectors from collinear to non-collinear and generate parametric fluorescence with varying conical emission angles.

The pump is a violet diode laser with a TEM_{00} linearly polarized 2-mm $1/e^2$ diameter output beam at a wavelength $\lambda_p = 405\text{ nm}$ (CNI Laser MLL-III-405). The pump beam is focused on the crystal through a lens (L1) with a focal length of 500 mm . Lens L1 and the objective are positioned to form a telescope such that the residual pump beam is collimated with a reduced beam radius below $100\mu\text{m}$. By passing the pump beam through a pair of a half-wave plate (HWP) and a Glan-Taylor polarizer (P1), we can vary the incident pump intensity by rotating the HWP while maintaining the degree of linear polarization better than 99.9%.

The angle-resolved images (Fig. 3) and spectra (Fig. 6) of parametric fluorescence are measured by a Fourier transform optical system, including a $20\times$ long-working-distance objective and an imaging spectrometer as shown in Fig. 1. The BBO crystal is positioned at the focal plane of the objective lens (effective focal length $f_o = 10\text{ mm}$). The parametric fluorescence with an amplitude distribution $F(x, y)$ at the crystal is collected by a $20\times$ microscope objective with a 10-mm effective focal length (numerical aperture N.A. = 0.26). The back focal plane of the objective is the Fourier transform plane with coordinates $(u, v) = (f_o \times \sin(\theta_x), f_o \times \sin(\theta_y))$. The collection angle is within $\pm 15^\circ$, limited by the objective. The objective lens converges parallel rays emanating from the crystal to the back focal plane of the objective. In this plane, the fluorescence image in the crystal is transformed into a far-field image in spatial frequency that is related to the emission angle

as described above. The spatial intensity distribution of parametric fluorescence in the back focal plane of the objective lens thus corresponds to the angular distribution of radiation. This Fourier transform plane is placed at the front focal plane of lens L2 (focal length $f = 100\text{ mm}$). Lenses L2 and L3 are identical and separated by a distance of $2f$, and they relay the Fourier transformed images to the entrance plane and then onto the charge-couple device (CCD) through the zero-order diffraction off the grating of the imaging spectrometer (PI-Acton SpectroPro 2750i, focal length 750 mm). In this way, we measure the angular distribution of parametric fluorescence. When lens L2 is removed, we project the real-space spatial intensity distribution of parametric fluorescence from the BBO crystal onto the CCD.

The fluorescence image is recorded by a CCD positioned in a conjugate imaging plane of the Fourier plane. The resultant intensity distribution is related to the Fourier transform of the intensity of the parametric fluorescence $I(x, y) = |F(x, y)|^2$. By projecting this far-field image through the entrance slit and the first-order diffraction of a 300 lines/mm grating, we obtain angle-resolved spectra as an image by taking the spectral dispersion of the parametric fluorescence as a function of angle. The spectral resolution of 0.1 nm is determined by the dispersion of the grating and the width of the entrance slit ($\approx 100\mu\text{m}$). The spatial and angular resolutions of the system are approximately $2\mu\text{m}$ and 2 mrad , respectively, limited by the pixel size of the liquid-nitrogen-cooled CCD camera.

In a parametric scattering process, only about one out of 10^{10} incident photons is parametrically down-converted. It is essential to prevent the transmitted and scattered pump photons from entering the spectrometer. For Type-I phase matching in a negative uniaxial BBO crystal (e-o-o case), the polarization of the high-frequency pump (e-wave) is orthogonal to the polarization of the signal and idler (o-waves). Thus, the transmitted and scattered pump photons can be suppressed by approximately 4–5 orders of magnitude by a pair of polarizers (P1 and P2) with orthogonal polarization orientations for pump and single/idler waves, respectively. The pump photons are further rejected by a thin-film notch filter (Semrock 405-nm StopLine single-notch filter) and two longpass filters (a Semrock 409-nm blocking edge BrightLine long-pass filter and a Schott GG435 glass filter). The filters are arranged in the sequence shown in Fig. 1 to suppress fluorescence from filters induced by the transmitted violet pump laser. The combination of polarizers and filters allows for a rejection of pump photons by approximately a factor of 10^{10} . This rejection ratio of 10^{10} can be further improved above 10^{14} by a miniature beam blocker made of a $\sim 0.5\text{ mm}$ -diameter silver-paste dot on a microscope cover positioned in front of the notch filter (NF)/objective. Depending on the signal wavelength, the measured angle-resolved spectra may still contain residual transmitted

and scattered pump and background fluorescence from filters. We measure such a background emission spectrum in the absence of Type-I e-o-o parametric fluorescence by rotating the BBO crystal 90 degrees azimuthally.

III. EXPERIMENTAL RESULTS AND MODELING

A. Phase Matching

The three-wave parametric processes are calculated according to the conservation of energy and momentum, commonly referred to as phase matching. The angle-resolved spectra of the parametric fluorescence are consistent with the tuning curves calculated for the phase-matching condition under a plane-wave approximation.

The energy conservation condition is expressed as

$$\omega_p = \omega_s + \omega_i, \quad (1)$$

where ω_p is the frequency of the incident pump wave and ω_s and ω_i are the frequencies of the signal and idler waves.

The momentum conservation condition can be expressed as

$$\mathbf{k}_p = \mathbf{k}_s + \mathbf{k}_i, \quad (2)$$

where \mathbf{k}_p , \mathbf{k}_s , and \mathbf{k}_i are the pump, signal, and idler wave vectors, respectively. For Type-I down-conversion in a BBO, the signal and idler labels are arbitrary. In the case of degenerate down conversion, $k_s = k_i$, and Eq. (2) reduces to

$$n_p = n_s \cos(\theta'_s), \quad (3)$$

where n_p and n_s are the indices of refraction of the pump and signal, and θ'_s is the angle formed by the propagation directions of the signal and pump waves inside the crystal.

We use a BBO crystal cut at an angle of $\theta_m = 29 \pm 0.5^\circ$, optimized for Type-I parametric down-conversion ($e \rightarrow o + o$). Down-converted signal/idler photons are co-linearly polarized but orthogonal to the polarization of the pump wave. The wavelengths and wave vectors of the parametric fluorescence are determined by the phase-matching angle θ_m , the angle formed by the optical axis of the crystal (z'-axis), and the wave vector of the pump wave (z-axis) as shown in Fig. 2. The crystals are mounted on a rotation stage such that the optical axis lies in a horizontal plane when the parametric fluorescence signal is maximized. By tilting the crystal, we can vary

the phase-matching condition from collinear to non-collinear, leading to a conical angle up to 5 degrees for degenerate parametric fluorescence near 810 nm.

For Type-I phase matching, the incident pump photons are subject to the extraordinary index of refraction $\tilde{n}(\theta_m)$, while the down-conversion photons are subject to the ordinary index of refraction. The extraordinary index of refraction, \tilde{n} , depends on the phase-matching angle θ_m and follows the relationship:

$$\tilde{n}(\theta_m, \lambda) = \left(\frac{\cos(\theta_m)^2}{n_o(\lambda)^2} + \frac{\sin(\theta_m)^2}{n_e(\lambda)^2} \right)^{-\frac{1}{2}}. \quad (4)$$

In the parametric process, a pump wave of wavelength λ_p creates signal waves at λ_s , and angles θ_s , subject to energy conservation (Eq. (1)) and momentum conservation (Eq. (2)). In the Type-I e-o-o case, $n_s = n_o(\lambda_s)$ and $n_p = \tilde{n}(\theta_m, \lambda_p)$ (Eq. 4). Here the labeling of signal and idler waves is arbitrary ($\theta_s = \theta_i$). A continuum of phase-matching functions $\Phi(\lambda_s, \theta_s)$ for parametric fluorescence can be obtained using the aforementioned equations and indices of refraction $n_o(\lambda_s)$ and $n_e(\lambda_s)$. Indices of refraction of wavelengths ranging from 0.3 μm to 5 μm are extracted from "NIST Noncollinear Phase Matching in Uniaxial and Biaxial Crystals Program" as described in Ref. [17]. We calculate the phase matching functions (tuning curves) for down-converted signal/idler waves ranging from 430 to 1000 nm for a pump wave $\lambda_p = 405$ nm.

B. Angle-Resolved Imaging

We adopt the plane-wave analysis developed in Refs. [7, 18, 19] to determine the angular distribution of parametric fluorescence. The effects of a finite pump beam size have also been considered in, for example, Refs. [20, 21]. Under a plane-wave approximation, the parametric fluorescence forms a conical angular distribution. The diameter and axis of the conical emission are determined by the wavelengths of the pump, signal, and idler waves, the Poynting vector walk-off angles of the three interacting waves, and the dispersion of the nonlinear crystal. In such a parametric process, the angular spread of the conical emission is determined by the conservation of transverse and longitudinal momenta of interaction waves. The transverse momentum induced by focusing the pump into the crystal contributes to a finite angular spread of the cones. By considering the longitudinal momentum, we deduce that parametric fluorescence signal is inversely proportional to the interaction length. In our experiments, we use a lens with a long focal length ($f = 500$ mm), resulting in a focal spot with a $1/e^2$ radius larger than $100\mu\text{m}$. Thus, for the experiments reported here, the effects of walk-off and finite pump beam size are negligible compared

with the spectral and angular resolution of the optical system.

We can determine the angular distribution of parametric fluorescence using the following phase-matching function for a finite crystal length L and a pump Gaussian beam profile with a $1/e^2$ radius W [17, 22, 23]:

$$\begin{aligned}\Phi &= \exp\left(-\frac{1}{2}W^2(\Delta k_x^2 + \Delta k_y^2)\right) \cdot \left(\frac{\sin(\frac{1}{2}L\Delta k_z)}{\frac{1}{2}L\Delta k_z}\right)^2 \\ &= \exp\left(-\frac{1}{2}\kappa^2W^2\right) \cdot \text{sinc}^2\left(\frac{1}{2}L\Delta k_z\right).\end{aligned}\quad (5)$$

The mismatch wave vector, $\Delta\mathbf{k}$, is decomposed into longitudinal ($\hat{z} \parallel \mathbf{k}_p$) and transverse (in x-y plane) parts: Δk_z and $\kappa = \sqrt{\Delta k_x^2 + \Delta k_y^2}$. The phase-matching tolerances can be considered in terms of the angular spread ($\Delta\theta_s$) and spectral bandwidth ($\Delta\lambda_s$), defined as the full-width-at-half-maximum (FWHM) for the above function. For a pump wave with a focal radius $W \approx 50\mu\text{m}$, only the tolerances from the sinc^2 part can be measured in our optical system. For this situation, considering a Taylor series expansion of Δk_z near the perfect phase-matching point ($\Delta k_z = 0$), we can analytically deduce the angular spread ($\Delta\theta_{\text{FWHM}}$) and spectral bandwidth ($\Delta\lambda_{\text{FWHM}}$) for the degenerate case ($k_s = k_i$):

$$\Delta\theta_{\text{FWHM}}(\theta_s) = \frac{2 \times 0.886 \pi}{L \times |\partial\Delta k_z / \partial\theta_s|} \approx \frac{2.783 \times n_s}{L \times k_s \times \theta_s}, \quad (6)$$

and

$$\Delta\lambda_{\text{FWHM}}(\lambda_s) = \frac{2 \times 0.886 \pi}{L \times |\partial\Delta k_z / \partial\lambda_s|} \approx \frac{0.443 \times \lambda_s^2}{L \times n_s \cos(\theta_s/n_s)},$$

where $\Delta k_z = |k_p' - 2k_s' \cos(\theta_s')|$, $k_s' = n_s\omega_s/c = 2\pi n_s/\lambda_s$, and $\theta_s \ll 1$.

The parametric fluorescence signal of angle-resolved images at $\lambda = 810$ nm are shown in Fig. 3. These false-color images, taken through a 1-nm band-pass filter, represent the angular intensity distributions of parametric fluorescence at $\lambda = 810 \pm 0.5$ nm for the phase-matching angle $\theta_m = 28.6^\circ$, 28.8° , 29.1° , and 29.4° . The BBO crystal is cut at the designed angle with about 1° tolerance. To determine the phase-matching angle θ_m with better precision, we first set the phase-matching angle for the collinear case by comparing the simulated and experimental angular distributions. We then deduce the phase-matching angle for the non-collinear case from the tilting angle of the crystal relative to that for the collinear case. The conical signal angle (θ_s) of degenerate parametric fluorescence at $\lambda = 810$ nm increases with θ_m . In Fig. 4, we plot the angular spread ($\Delta\theta_{\text{FWHM}}$)

as a function of the inverse of the signal angle ($1/\theta_s$). The angular spread decreases with θ_s for small angles when $\sin(\theta_s) \approx \theta_s$. We attribute the discrepancy between experimental data and Eq. (6) to a limited experimental angular resolution (≈ 2 mrad), finite pump beam size and spatial coherence, and the birefringent walk-off.

C. Angle-Resolved Spectroscopy

The parametric fluorescence flux per unit frequency is

$$N_s(\omega_s, \boldsymbol{\kappa}_s) = \frac{\hbar d_{eff}^2 \omega_s \omega_i \omega_p L^2 N_p}{2\pi^4 c^3 \epsilon_0 n_s n_i n_p} d\omega_s d^2 \boldsymbol{\kappa}_s \int d^2 \boldsymbol{\xi} \exp(\frac{1}{2} \xi^2) \cdot \text{sinc}^2 \left(\frac{1}{2} L \Delta k_z \right), \quad (7)$$

where d_{eff} is the effective second-order nonlinear coefficient, L the interacting crystal length, $N_p = P_p/\hbar\omega_p$ the pump flux, $\boldsymbol{\xi} = \boldsymbol{\kappa}W = (\boldsymbol{\kappa}_s + \boldsymbol{\kappa}_i)W$ the dimensionless transverse momentum associated with the signal and idler waves, and W the $1/e^2$ pump beam radius. The integration over $\boldsymbol{\xi}$ is detailed in Appendix.

Experimental angle resolved spectra $N_s^*(\lambda_s, \theta_s)$ and corresponding calculated $N_s(\lambda_s, \theta_s)$ are shown in Fig. 6 (e)–(h). The tuning curves, corresponding to the perfect phase-matching condition, are shown as white dashed lines on the experimental spectra. The experimental parameters are $N_p = 1.63 \times 10^{17}$ /s ($P_p = 80$ mW), $L=3$ mm, and $W^2 = 60\mu\text{m} \times 30\mu\text{m}$. The indices of refraction n_s , n_i , and n_p are evaluated using the database in Ref. [17] ($n_{s,i} \approx 1.66$ at 810 nm). The effective nonlinear coefficient of a BBO crystal can be deduced from its d-matrix using $d_{eff} = d_{31} \sin(\theta_m + \rho) - d_{22} \cos(\theta_m + \rho) \sin(3\phi)$ for Type-I phase matching. θ_m is the phase-matching angle, ϕ the azimuthal angle, and ρ the birefringent walk-off angle. We use $d_{eff}=1.75$ pm/V for 405 nm adopting from Refs. [4, 13, 24].

Computationally, the angular distributions of parametric fluorescence are calculated for signal wavelengths from 430 to 1000 nm with step size $\delta\lambda = 1$ nm and $\delta\theta_s = 0.03^\circ \approx 0.5$ mrad. Selected calculated angular distributions of fluorescence flux per 1 nm are shown in Fig. 6 (e)–(h) for $\theta_m = 28.6^\circ, 28.8^\circ, 29.1^\circ, 29.4^\circ$. The shortest signal wavelength appears in the simulation is ≈ 440 nm, limited by the availability of refractive indices between $\lambda = 0.3\mu\text{m}$ and $5\mu\text{m}$ [25]. Experimentally, parametric fluorescence with a wavelength as short as 431 nm can be observed near $\theta_s = 0$.

The experimental angle-resolved parametric fluorescence images are shown in the left panel of Fig. 6. These images are taken through a notch filter and longpass filters (cutoff wavelength of 420 nm) as shown in Fig. 1. Experimental angle-resolved spectra are acquired by spectrally resolving

the parametric fluorescence across the fluorescence cone center through the entrance slit with an opening of $100\text{ }\mu\text{m}$, corresponding to $\Delta\theta_x \approx 0.6^\circ$. Angle-resolved fluorescence images (Fig. 6(a)–(d), left panel) are taken for the zero-order diffraction of a holographic grating with 1800 lines/mm, while angle-resolved spectra (right panel) are dispersed by a grating with 300 lines/mm and a blaze wavelength of 1000 nm. The angular resolution is about 2 mrad, while the spectral resolution is about 0.1 nm. Residual stray or scattered pump laser light can be measured by rotating the BBO crystal 90° azimuthally. Such background ‘noise’ is subtracted. Note that the measured CCD intensity is subject to the nonuniform spectral sensitivity and collection efficiency of the optical system including the effects of lens coating, optical filters, and gratings, and the spectral response of the CCD camera. The spectra branches out from $\theta_s = 0$ at $\lambda \approx 433\text{ nm}$. The secondary weak arcs in the wavelength range above 870 nm outside of the expected parametric fluorescence peaks are due to the second-order diffraction of the grating for the fluorescence from approximately 435 nm to 500 nm. The inner arcs branching from 435 nm and closing near 530 nm are due to parametric fluorescence from a Type-II parametric process ($e \rightarrow o + e$). The turning curves for such Type-II parametric fluorescence are indicated by black dashed-dotted lines in experimental spectral images.

D. Fluorescence Photon Flux

The integrated parametric fluorescence photon flux can be obtained by the integrating over ξ and κ_s in Eq. (7). For values of θ_m or ω_s such that the parametric fluorescence cone has a radius sufficiently large with negligible emission at the cone center, the resultant integrated fluorescence flux is [18]

$$\begin{aligned} N_s &= \frac{\hbar d_{eff}^2 L \omega_s^2 \omega_i^2}{\pi c^4 \epsilon_0 n_p^2} N_p d\omega_s \\ &= (2\pi)^4 \frac{2\hbar c d_{eff}^2 L}{\epsilon_0 n_p^2 \lambda_s^4 \lambda_i^2} N_p d\lambda_s. \end{aligned} \quad (8)$$

The efficiency $\eta_s \equiv N_s/N_p$ is a coefficient depending largely on the material properties such as the second-order nonlinear coefficient, interacting crystal length, and index of refraction for the pump wave. Assuming a bandwidth $\Delta\lambda = 1\text{ nm}$ and $L = 3\text{ mm}$, the efficiency coefficient $\eta_s = 1.3 \times 10^{-10}$ for the degenerate parametric fluorescence at $\lambda_s = 810\text{ nm}$ under $\lambda_p = 405\text{ nm}$. Specifically, we evaluate η_s for $\theta_m = 29.12^\circ$ (Fig. 6g). We integrate the photon flux of simulated angle-resolved spectra for $\lambda_s = 809.5 \rightarrow 810.5\text{ nm}$, $\theta_s = 0 \rightarrow 7.5^\circ$, and $\phi = 0 \rightarrow 2\pi$. The total parametric fluorescence photon flux, including both degenerate signal and idler waves, is $2 N_s \approx 4.2 \times 10^7/s$.

The wavelength of parametric fluorescence generated here ranges from ≈ 430 nm to above 1000 nm. The collection efficiency and spectral response of the optical systems could vary more than an order of magnitude in such a broad wavelength range. Therefore we consider the degenerate parametric fluorescence at $\lambda = 810$ nm to compare the experimentally determined fluorescence photon flux with the theoretically integrated photon flux (see Eq. (8)).

The integrated degenerate parametric fluorescence flux at $\lambda_s = 810$ nm as a function of the incident pump flux are shown in Fig. 5. First, we determine the overall collection efficiency and the spectral response of the imaging and spectroscopy system by passing a laser beam of $\lambda = 810$ nm with a known photon flux through the same optical path as the parametric fluorescence. We then integrate the signal in angle-resolved images as shown in Fig. 3. Taking into account the system response at $\lambda = 810$ nm, we can determine the absolute fluorescence flux experimentally within roughly 20% error. The relative fluorescence fluxes, determined by the linearity of the CCD camera, is within 1% error. The absolute value of pump flux is within roughly 10% error. The relative pump fluxes, as varied by a combination of a half-wave plate and a polarizer and limited by the linearity of the power meter, are known within a few percent. Thus we can investigate the pump flux (power) dependence of parametric fluorescence flux with precision. Fluorescence signal flux is linearly proportional to the pump flux over two order of magnitude, confirming that the dominant signal is *spontaneous* parametric fluorescence as described by Eq. (8). The slopes correspond to the efficiency coefficients. Considering both signal and idler fluorescence, we determined $\eta = 2\eta_s$ to be approximately 2.8×10^{-10} . Experimental and theoretical values of $\eta = 2\eta_s$ for selected phase-matching angles are listed in Table I.

E. Instrument Spectral Response Function

Parametric fluorescence spectra can also be used to calibrate the instrument spectral response function (ISRF) of the imaging spectroscopy system. According to Eq. (8), which is valid for non-collinear cases, we can deduce a parameter $S \equiv N_s \times \lambda_s^4 \lambda_i^2 = 2(2\pi)^4 \hbar c d_{eff}^2 L N_p d\lambda_s / (\epsilon_0 n_p^2)$ [18]. S is a wavelength-independent constant for a given pump wavelength and geometry. We define a generalized spectral function, $S(\lambda_s) \equiv N_s(\lambda_s) \lambda_s^4 \lambda_i^2$, for both calculated and experimental angle-resolved spectra. The calculated $S_{sim}(\lambda_s)$ exhibit less than 1% variation between $\lambda = 460$ and 1000 nm. Experimentally, $S_{exp}^*(\lambda_s) = N_s^*(\lambda) \lambda_s^4 \lambda_i^2$ can be determined from the integration of an angle-resolved spectrum $N_s^*(\lambda, \theta_s)$ over θ_s . $S_{exp}(\lambda)$ represents the relative ISRF of the imaging spectroscopy system, including the optical components, grating, and CCD camera along the fluo-

rescence collection optical path. The value of the ISRF at a fixed wavelength can then be used to determine the absolute ISRF across the parametric fluorescence wavelength range. The effective efficiency, defined as (# of photo-generated electrons / # of photons), is $\approx 20\%$ at $\lambda = 810$ nm in our experiments. $S_{exp}^*(\lambda)$ and $S_{sim}(\lambda)$ for phase-matching angles $\theta_m = 29.1^\circ$ and 29.4° are shown in Fig. 7. The stray scattered pump laser signal becomes increasingly difficult to subtract from these angle-resolved spectra, leading to a distorted $S_{exp}^*(\lambda)$. We thus use $S_{exp}^*(\lambda)$ at $\theta_m = 29.1^\circ$ to deduce the ISRF of our optical setup shown in Fig. 1.

Acknowledgments

We thank Brage Golding and John A. McGuire for discussions. This work was supported by grant DMR-0955944 from the National Science Foundation and by internal Strategic Initiative Projects of the College of Natural Science at Michigan State University.

IV. APPENDIX: CALCULATION OF FLUORESCENCE FLUX

Here we describe the integration over $\boldsymbol{\xi}$ of Eq. (7) for the calculation of the angular distribution of fluorescence flux here. The mismatch wave vector $\Delta\mathbf{k} = \mathbf{k}'_s + \mathbf{k}'_i - \mathbf{k}'_p$ can be decomposed into longitudinal ($\Delta k_z \hat{z}$) and transverse ($\boldsymbol{\kappa}$) parts:

$$\begin{aligned}\Delta k_z &= k'_{sz} + k'_{iz} - k'_{pz} \\ &= \sqrt{k'^2_s - \kappa_s^2} + \sqrt{k'^2_i - \kappa_i^2} - k'_{pz}, \text{ and} \\ \boldsymbol{\kappa} &= \boldsymbol{\kappa}_s + \boldsymbol{\kappa}_i.\end{aligned}$$

Here $k'_s = n_s \omega_s / c$, $k'_i = n_i \omega_i / c$, and $k'_p = n_p \omega_p / c$ are the wave numbers for the signal, idler, and pump, respectively. $\boldsymbol{\kappa}_s$ ($\boldsymbol{\kappa}_i$) is the transverse wave vector of the signal (idler) wave. The phase-matching function Φ in Eq. (5) is a function of three variables: ω_s , $\boldsymbol{\kappa}_s$ and $\boldsymbol{\kappa}_i$. Considering energy conservation $\omega_p = \omega_s + \omega_i$, we can carry out the integration over $\boldsymbol{\xi}$ for two independent variables, ω_s and $\boldsymbol{\kappa}_s$. Using $\boldsymbol{\xi} = \boldsymbol{\xi}_s + \boldsymbol{\xi}_i = (\boldsymbol{\kappa}_s + \boldsymbol{\kappa}_i) W$, we rewrite Eq. (7) as

$$N_s(\omega_s, \boldsymbol{\kappa}_s) = \frac{\hbar d_{eff}^2 \omega_s \omega_i \omega_p L^2 N_p}{8\pi^4 c^3 \epsilon_0 n_s n_i n_p} d\omega_s d^2\boldsymbol{\kappa}_s \int d^2\boldsymbol{\xi}_i \exp\left(-\frac{1}{2}|\boldsymbol{\xi}_s + \boldsymbol{\xi}_i|^2\right) \cdot \text{sinc}^2\left(\frac{1}{2}L\Delta k_z\right)$$

We further simplify the numerical integration by (a) considering that the sinc^2 term is a constant for a given set of ω_s and $\boldsymbol{\kappa}_s$, and (b) applying a saddle-point approximation.

κ_s and κ_i form an angle φ in the $x-y$ plane of the crystal, where $\varphi = 0$ in the anti-parallel case. Under a pump wave vector along \hat{z} , the phase-matching condition is met mostly for $\mathbf{k}'_s + \mathbf{k}'_i = 0$; i.e., $\varphi \approx 0$. The Gaussian term of the integrand can thus be separated and integrated with a saddle-point approximation for $\varphi \approx 0$ and $\xi_s \approx \xi_i$:

$$\begin{aligned} \int d^2 \boldsymbol{\xi}_i \exp \left(-\frac{1}{2} (\xi_s^2 + \xi_i^2 - 2 \xi_s \xi_i \cos(\varphi)) \right) &\approx \int \xi_i d\xi_i \exp \left(-\frac{1}{2} (\xi_s - \xi_i)^2 \right) \int d\varphi \exp \left(-\frac{1}{2} \xi_s \xi_i \varphi^2 \right) \\ &\approx \sqrt{2\pi} \int d\xi_i \exp \left(-\frac{1}{2} (\xi_s - \xi_i)^2 \right). \end{aligned}$$

The integrand is a maximum at $\xi_s = \xi_i$, where pairs of signal and idler photons are emitted in approximately opposite conical directions. Applying the above two approximations, we obtain

$$N_s(\omega_s, \kappa_s, \phi) = \frac{\hbar d_{eff}^2 \omega_s \omega_i \omega_p L^2 N_p}{8\pi^4 c^3 \epsilon_0 n_s n_i n_p} \sqrt{2\pi} d\omega_s \kappa_s d\kappa_s d\phi \int d\xi_i e^{-\frac{1}{2}(\xi_s - \xi_i)^2} \cdot \text{sinc}^2 \left(\frac{1}{2} L \Delta k_z \right),$$

where $d^2 \kappa_s = \kappa_s d\kappa_s d\phi$, ϕ is the azimuthal angle.

$N_s(\omega_s, \kappa_s, \phi)$ is isotropic in ϕ . It can be expressed as $N_s(\lambda_s, \theta_s)$, a function of experimentally measurable signal angle θ_s and wavelength λ_s by considering that $\kappa_s = k_s \sin \theta_s$ and $\omega_s = 2\pi c/\lambda_s$:

$$N_s(\lambda_s, \theta_s) = \frac{2\pi \sqrt{2\pi} \hbar d_{eff}^2 \omega_p L^2 N_p}{\epsilon_0 n_s n_i n_p \lambda_s^5 \lambda_i} \sin(2\theta_s) d\lambda_s d\theta_s \int d\xi_i e^{-\frac{1}{2}(\xi_s - \xi_i)^2} \cdot \text{sinc}^2 \left(\frac{1}{2} L \Delta k_z \right). \quad (9)$$

The equation for $N_s(\lambda_s, \theta_s)$ above, together with $\omega_p = \omega_s + \omega_i$ and $\mathbf{k}_p = \mathbf{k}_s + \mathbf{k}_i$, is used in the numerical integration to obtain the theoretical angular distribution of parametric fluorescence shown in Fig. 6.

-
- [1] Y. H. Shih and C. O. Alley, Phys. Rev. Lett. **61**, 2921 (1988), URL <http://link.aps.org/doi/10.1103/PhysRevLett.61.2921>.
 - [2] Y. H. Shih, A. V. Sergienko, M. H. Rubin, T. E. Kiess, and C. O. Alley, Phys. Rev. A **50**, 23 (1994), URL <http://link.aps.org/doi/10.1103/PhysRevA.50.23>.
 - [3] P. G. Kwiat, K. Mattle, H. Weinfurter, A. Zeilinger, A. V. Sergienko, and Y. Shih, Phys. Rev. Lett. **75**, 4337 (1995), URL <http://link.aps.org/doi/10.1103/PhysRevLett.75.4337>.
 - [4] Y. Shih and Y. Shih, Reports on Progress in Physics **66**, 1009 (2003), ISSN 0034-4885, URL <http://dx.doi.org/10.1088/0034-4885/66/6/203>.

- [5] W. H. Louisell, A. Yariv, and A. E. Siegman, Phys. Rev. **124**, 1646 (1961), URL <http://link.aps.org/doi/10.1103/PhysRev.124.1646>.
- [6] J. P. Gordon, W. H. Louisell, and L. R. Walker, Phys. Rev. **129**, 481 (1963), URL <http://link.aps.org/doi/10.1103/PhysRev.129.481>.
- [7] D. A. Kleinman, Phys. Rev. A **174**, 1027 (1968), URL <http://link.aps.org/doi/10.1103/PhysRev.174.1027>.
- [8] S. E. Harris, M. K. Oshman, and R. L. Byer, Phys. Rev. Lett. **18**, 732 (1967), URL <http://link.aps.org/doi/10.1103/PhysRevLett.18.732>.
- [9] T. G. Giallorenzi and C. L. Tang, Phys. Rev. **166**, 225 (1968), URL <http://link.aps.org/doi/10.1103/PhysRev.166.225>.
- [10] R. L. Byer and S. E. Harris, Phys. Rev. **168**, 1064 (1968), URL <http://link.aps.org/doi/10.1103/PhysRev.168.1064>.
- [11] M. M. Choy and R. L. Byer, Phys. Rev. B **14**, 1693 (1976), URL <http://link.aps.org/doi/10.1103/PhysRevB.14.1693>.
- [12] I. Shoji, T. Kondo, A. Kitamoto, M. Shirane, and R. Ito, JOSA B **14**, 2268 (1997), URL <http://dx.doi.org/10.1364/JOSAB.14.002268>.
- [13] I. Shoji, T. Kondo, and R. Ito, Optical and Quantum Electronics **34**, 797 (2002), URL <http://dx.doi.org/10.1023/A:1016545417478>.
- [14] B. Y. Zeldovich and D. N. Klyshko, JETP Letters **9**, 40 (1969), URL http://www.jetpletters.ac.ru/ps/1639/article_25275.shtml.
- [15] D. C. Burnham and D. L. Weinberg, Phys. Rev. Lett. **25**, 84 (1970), URL <http://link.aps.org/doi/10.1103/PhysRevLett.25.84>.
- [16] C. Chen, B. Wu, A. Jiang, and G. You, Sci. Sin. Ser. B **28**, 235 (1985).
- [17] N. Boeuf, D. Branning, I. Chaperot, E. Dauler, S. Guerin, G. Jaeger, A. Muller, and A. Migdall, Opt. Eng. **39**, 1016 (2000), ISSN 00913286, URL <http://dx.doi.org/10.1117/1.602464>.
- [18] K. Koch, E. C. Cheung, G. T. Moore, S. H. Chakmakjian, and J. M. Liu, IEEE Journal of Quantum Electronics **31**, 769 (1995), ISSN 00189197, URL <http://dx.doi.org/10.1109/3.375922>.
- [19] C. K. Hong and L. Mandel, Physical Review A **31**, 2409 (1985), URL <http://link.aps.org/doi/10.1103/PhysRevA.31.2409>.
- [20] A. Ling, Lamas-Linares, and C. Kurtsiefer, Phys. Rev. A **77**, 043834 (2008), URL <http://link.aps.org/doi/10.1103/PhysRevA.77.043834>.
- [21] M. W. Mitchell, Phys. Rev. A **79**, 043835 (2009), URL <http://link.aps.org/doi/10.1103/PhysRevA.79.043835>.
- [22] M. H. Rubin, Phys. Rev. A **54**, 5349 (1996), URL <http://link.aps.org/doi/10.1103/PhysRevA.54.5349>.
- [23] M. Fedorov, M. Efremov, P. Volkov, E. Moreva, S. Straupe, and S. Kulik, Physical Review A **77**, 1 (2008), ISSN 1050-2947, URL <http://link.aps.org/doi/10.1103/PhysRevA.77.032336>.

- [24] R. S. Klein, G. E. Kugel, A. Maillard, A. Sifi, and K. Polgár, *Optical Materials* **22**, 163 (2003), ISSN 0925-3467, URL [http://dx.doi.org/10.1016/S0925-3467\(02\)00360-9](http://dx.doi.org/10.1016/S0925-3467(02)00360-9).
- [25] A. Migdall, *Optical Engineering* **39**, 1016 (2000), ISSN 00913286, URL <http://dx.doi.org/10.1117/1.602464>.

TABLE I: Parametric fluorescence efficiency $\eta = 2N_s/N_p$ for 810 ± 0.5 nm

θ_m	Exp.	Sim. [Eq. (9)]	Th. [Eq. (8)]	n_p
28.6°	1.3×10^{-10}	2.5×10^{-11}	—	1.6612
28.8°	2.8×10^{-10}	2.5×10^{-10}	2.6×10^{-10}	1.6608
29.1°	2.7×10^{-10}	2.6×10^{-10}		1.6602
29.4°	2.7×10^{-10}			1.6599

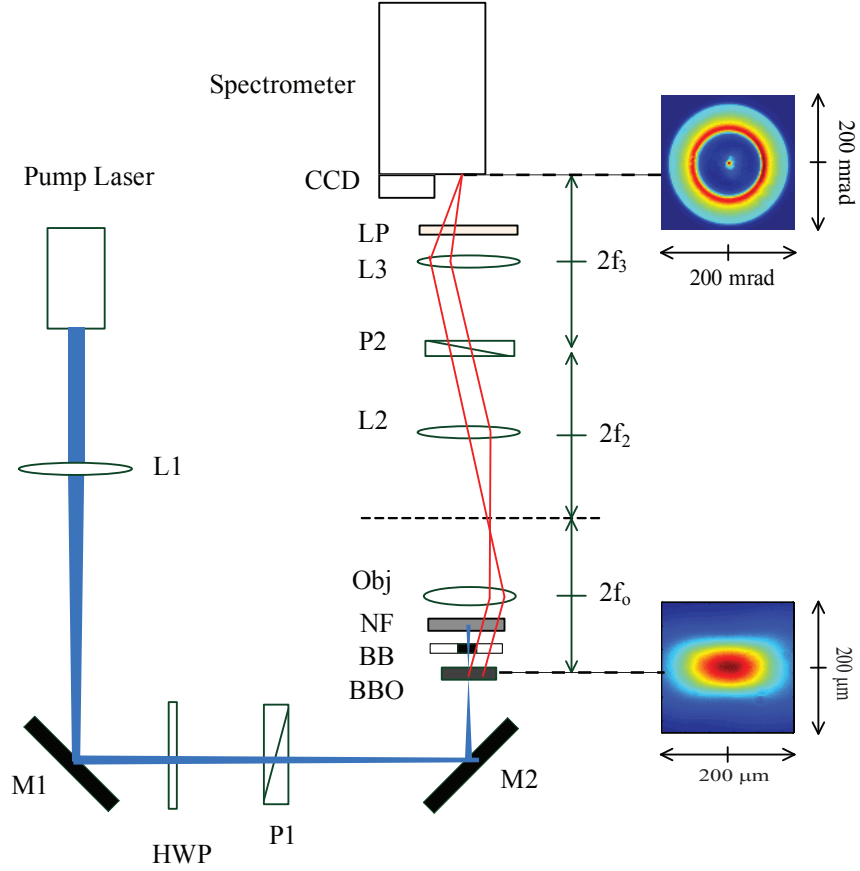


FIG. 1: **Schematic diagram of the experimental setup.** The transmitted and scattered pump photons are rejected by a miniature beam blocker, a thin-film notch filter, and long-pass filters. The angular and spectral distributions of conical parametric fluorescence are measured by an imaging spectrometer through a Fourier transform optical system. L1, L3 and L4 are convergent lenses with focal length $f = 500, 100$, and 100 mm, respectively; L2 is an objective ($20\times$ N.A.=0.26) with an effective focal length of 10 mm (Mitutoyo Plan Apo infinity-corrected long-working-distance objective); P1 and P2 are Glan–Taylor and Glan–Thompson polarizers; M1 and M2 are silver mirrors; HWP is a half-wave plate for $\lambda = 405$ nm; BB is a miniature pump beam blocker; NF is a notch filter (Semrock 405-nm StopLine single-notch filter); and LP represents longpass filters (a Semrock 409-nm blocking edge BrightLine long-pass filter and a Schott GG435 glass filter). When L2 is removed, a real-space fluorescence image is formed at the entrance of the spectrometer with an imaging magnification of $10\times$. Examples of real-space and angle-resolved fluorescence images are shown with actual dimensions.

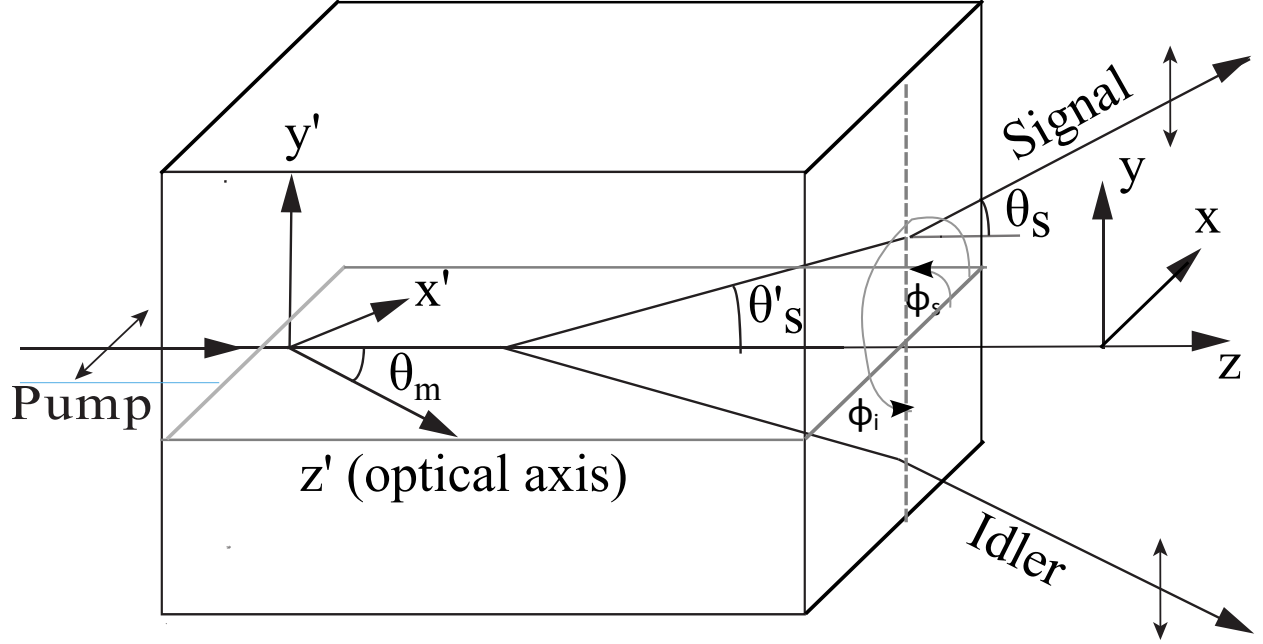


FIG. 2: Schematic diagram of the crystal and laboratory frame coordinates for parametric down-conversion in a BBO crystal. The phase-matching angle θ_m is defined as the angle formed by the crystal optical axis (z') and the pump wave vector (z). The angles θ'_s and θ_s are, respectively, internal and external angles formed by the signal and pump wave vectors. Here the incident pump wave is horizontally polarized, leading to a vertically polarized down-converted signal and idler waves.

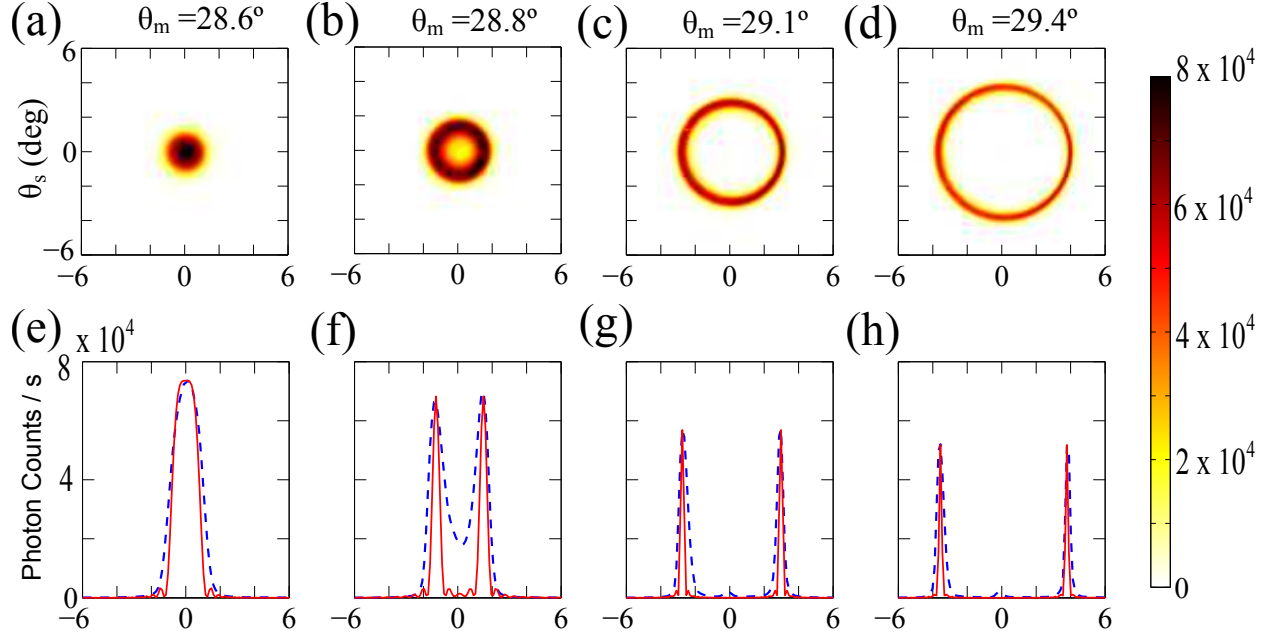


FIG. 3: **Angular intensity distribution of parametric fluorescence at 810 nm.** (a)–(d) Angle-resolved images of parametric fluorescence for $\lambda = 810 \pm 0.5$ nm and θ_m as indicated. The external angle θ_s is formed by the pump and signal wave vectors in air (see also Fig. 2). The color palette represents the intensity of the single radiation. Parametric fluorescence is spectrally filtered through a 1-nm bandpass filter with central wavelength $\lambda = 800$ nm. The phase-matching angle is adjusted by tilting the BBO crystal with respect to the pump wave vector. The collinear phase-matching angle is set to $\theta_m = 28.6^\circ$ according to a theoretical calculation using indices of refraction given in Ref. [17]. (e)–(g) Experimental (blue dashed line) and theoretical (red solid line) cross-sections. The non-collinear phase-matching angle relative to the collinear one can be determined experimentally by measuring the tilting angle of the crystal surface with respect to the pump wave vector.

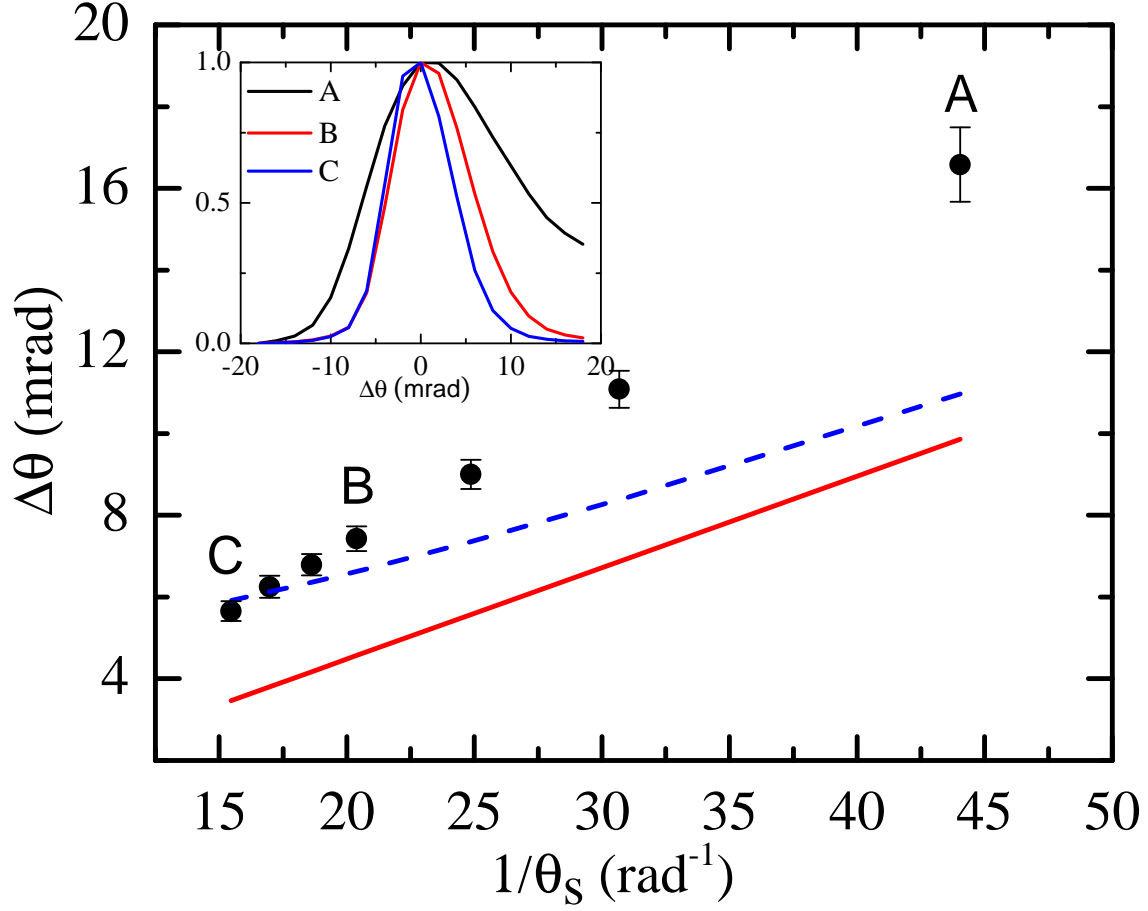


FIG. 4: **Angular spreads $\Delta\theta_{\text{FWHM}}$ of parametric fluorescence at 810 nm.** $\Delta\theta_{\text{FWHM}}$ is plotted as a function of the inverse of the signal angle ($1/\theta_s$). Experimental data are represented with error bars as solid circles. The red solid line is the theoretical curve according to Eq. 6, while the dashed line is the theoretical curve including a finite angular resolution of 2 mrad. Selected experimental angular intensity profiles for A ($\theta_s = 1.3^\circ = 0.023$ rad), B ($2.8^\circ = 0.049$ rad), and C ($3.7^\circ = 0.065$ rad) are shown in the inset.

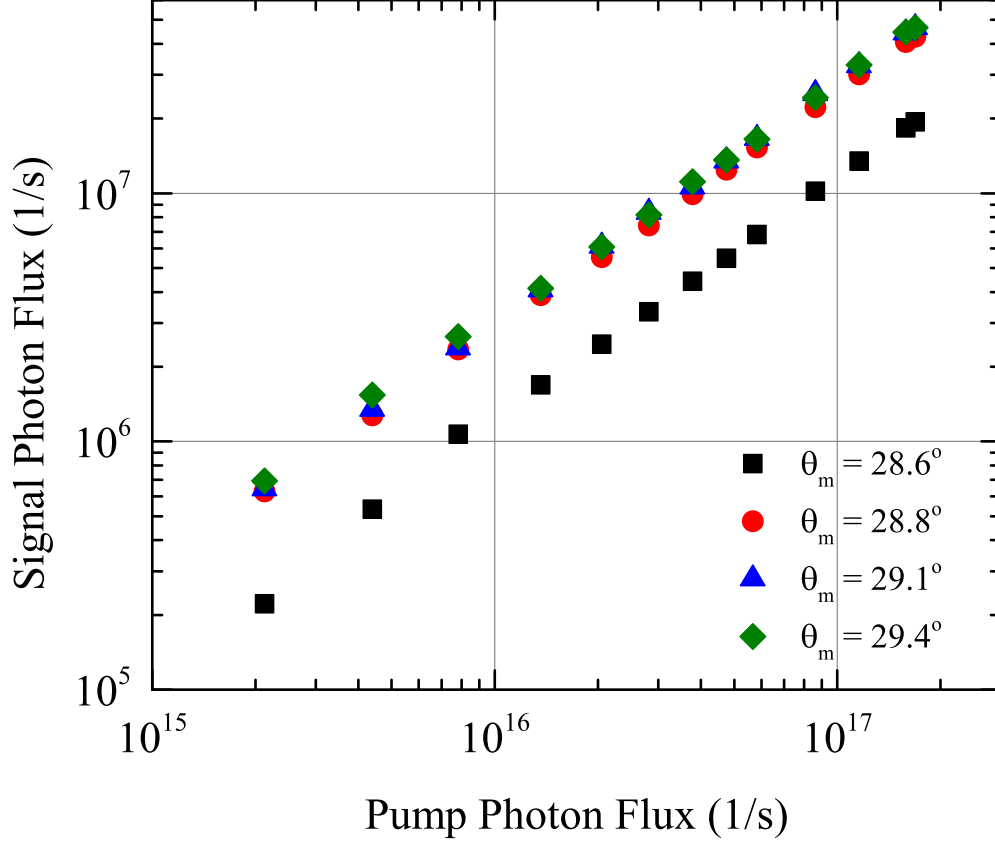


FIG. 5: **Parametric fluorescence flux at 810nm.** Integrated degenerate parametric fluorescence flux at $\lambda_s = 810$ nm as a function of the incident pump flux for the collinear case and three phase-matching angles θ_m of the angle-resolved images shown in Fig. 3. Signal flux is linearly proportional to the pump flux over two order of magnitude, confirming that the dominant signal is *spontaneous* parametric fluorescence as described by Eq. (8). The slopes $\eta = N_s/N_p$ are 1.16×10^{-10} for $\theta_m = 28.6^\circ$, 2.6×10^{-10} for $\theta_m = 28.8^\circ$, and 2.8×10^{-10} for $\theta_m = 29.1^\circ$ and 29.4° .

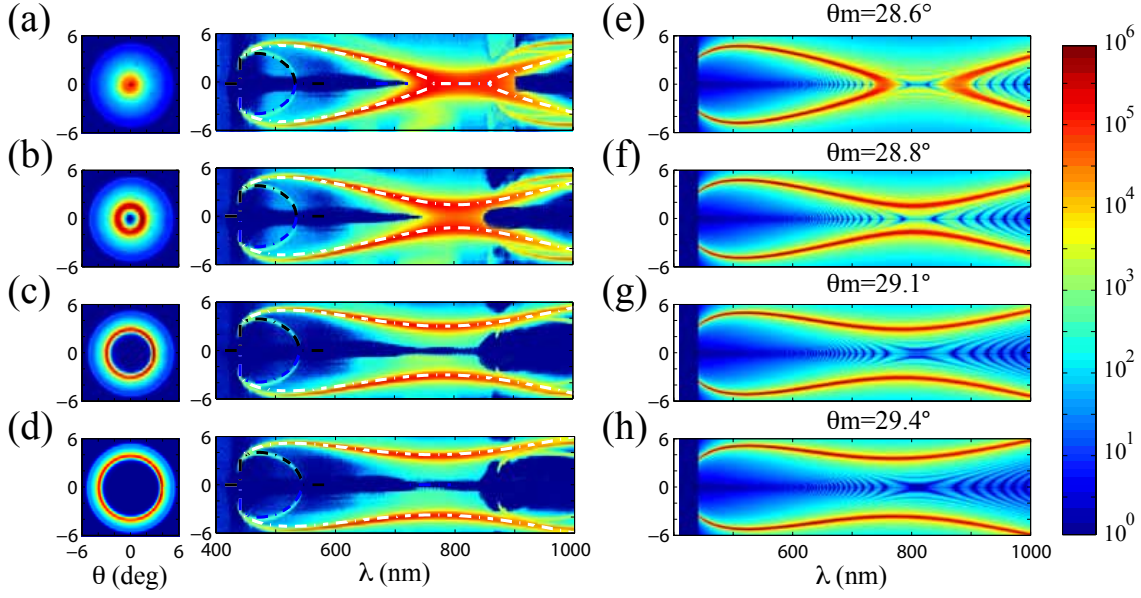


FIG. 6: **Angle-resolved spectra of parametric fluorescence.** (a)-(d) Experimental angle-resolved parametric fluorescence images (left panel) and spectra (right panel) for a phase-matching angle $\theta_m = 28.6^\circ, 28.8^\circ, 29.1^\circ$, and 29.4° , respectively. (e)-(h) Theoretical fluorescence flux calculated according to Eq. (7) (see also Appendix). The tuning curves for the perfect phase-matching condition are indicated by the white dashed lines on experimental imaging spectra. The color palette represents the calculated photon flux with $\Delta\lambda_s = 1$ nm and $\Delta\theta_s = 0.5$ mrad on a logarithmic scale.

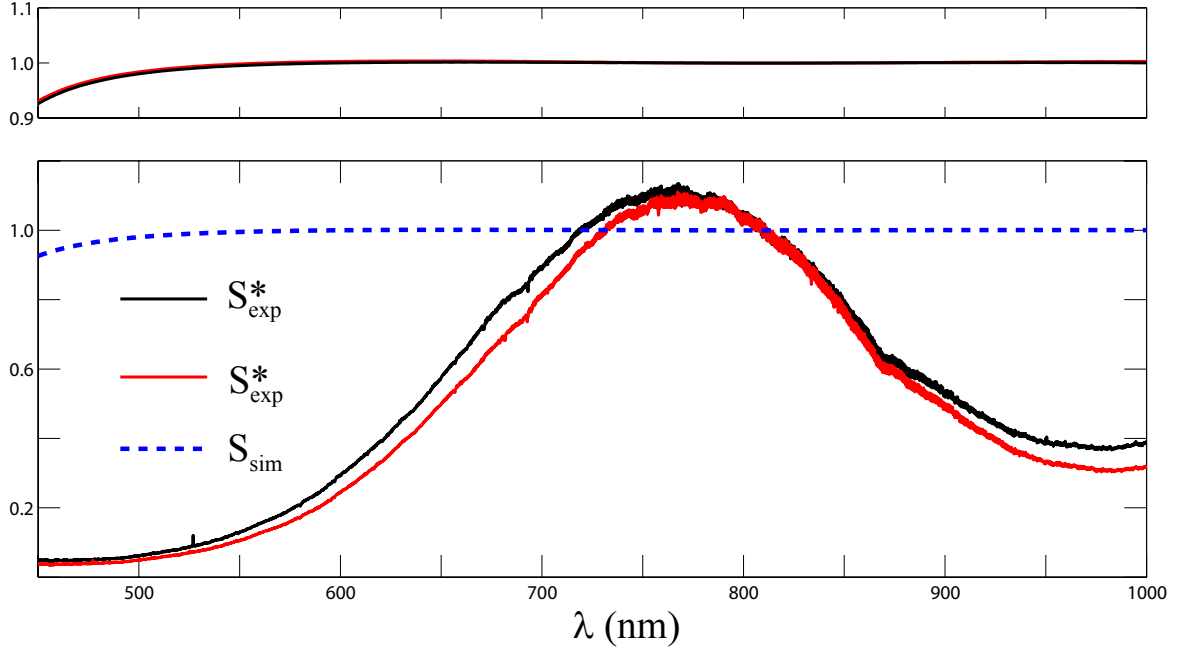


FIG. 7: Instrument spectral response function. The normalized spectral density function $S(\lambda)$ for $\theta_m = 29.1^\circ$ and 29.4° . S_{sim} is determined from the integration over $\theta_s = -7.5$ to 7.5° of the calculated angle-resolved spectra as shown in Fig. 6 (Eq. (7)). The black and red curves are S_{sim} or S_{exp}^* for $\theta_m = 29.4^\circ$ and 29.1° , respectively. The value of S_{sim} is a constant with 1% standard deviation across wavelengths from 500 to 1000 nm, validating the calculated angular fluorescence spectra and Eq. (8). $S_{exp}^*(\lambda) = N_s^*(\lambda) \lambda_s^4 \lambda_i^2$, where $N_s^*(\lambda)$ is the integration over $\theta_s \approx -15$ to 15° of the experimental imaging spectra $N_s^*(\lambda_s, \theta_s)$. $S_{exp}^*(\lambda)$ represents a relative instrument spectral response function (ISRF) of the optical spectroscopy system, including optical filters and a Glan-Thompson polarizer along the path of the fluorescence, a liquid-nitrogen-cooled CCD (PI-Acton Spec-10:400BR), and a 300g/mm plane ruled reflectance grating with 1000-nm blaze wavelength (PI-Acton 750-1-030-1). The polarization of the fluorescence is vertically polarized. The absolute ISRF (or collection efficiency) can be deduced by calibrating $S_{exp}^*(\lambda)$ at a fixed wavelength such as $\lambda = 810$ nm in our experiments.